# Lithiation Confined in One Dimensional Nanospace of TiO$_2$ (Anatase) Nanotube to Enhance the Lithium Storage Property of CuO Nanowires

Ang Li, Huaihe Song,[*] Xiaohong Chen, Jisheng Zhou, and Zhaokun Ma

State Key Laboratory of Chemical Resource Engineering, Beijing Key Laboratory of Electrochemical Process and Technology for Materials, Beijing University of Chemical Technology, Beijing 100029, P.R. China

**S** *Supporting Information*

**ABSTRACT:** We have fabricated CuO@TiO$_2$ nanocable arrays by a facile method involving in situ thermal oxidation of Cu foil and coating of tetrabutyl titanate solution. The structure of the nanocables has been investigated by various techniques to comfirm that the cores are mainly crystalline monoclinic CuO, and the shells are crystalline tetragonal anatase TiO$_2$. When used as an anode material for lithium-ion batteries, the nanoconfinement effect plays an important role in improving the lithium-ion storage preformance: the lithiation will be confined in one-dimensional space of TiO$_2$ nanotubes to limit the pulverization of CuO, and the phase interface will cause an interfacial adsorption to enrich more lithium ions at some level. Benefiting from the nanoconfinement effect and interfacial adsorption, the reversible capacity does not fade, but rather increases gradually to 725 mAh g$^{-1}$ after 400 cycles at a current density of 60 mA g$^{-1}$, superior to the theoretical capacity of CuO.



**KEYWORDS:** nanocable arrays, CuO, TiO$_2$, lithium ion battery anodes, nanoconfinement effect, interfacial adsorption
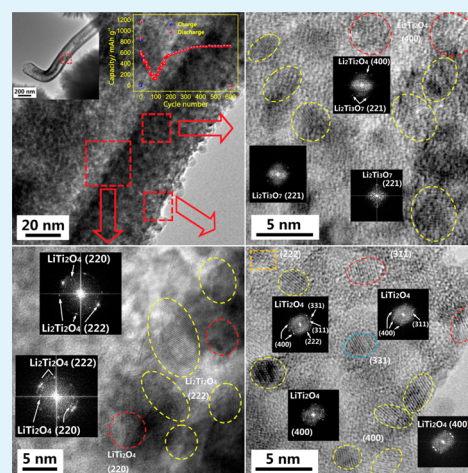
## ■ INTRODUCTION

Due to their high theoretical capacities and low cost, transition metal oxides have attracted continuous interest as anode materials for lithium-ion batteries.[1−3] However, the poor electrical conductivity and large volume change result in bad cyclic stability and low reversible capacity.[4] In order to solve these problems, scientists usually use nanocrystallization and/or composite processes to improve the lithiation performances of transition metal oxides.[5,6] Encapsulated nanostructures,[2,4,7] carbon nanostructure loaded materials,[8−10] and hollow nanostructures[4,11,12] are the most widely used strategies, which have enhanced the cyclic stability and reversible capacity of transition metal oxides. In many cases, an interesting phenomenon was observed that the specific capacities of some composite electrode systems did not fade, but rather increased after the initial cycles even higher than their theoretical capacities, for example Cu nanowires@Fe$_3$O$_4$,[13] MoO$_2$ nanospheres@C,[14] α-Fe$_2$O$_3$ nanoplatelets/N-doped graphene,[8] and MnO nanowire/graphene.[9] To explain the outstanding cyclic performances, several possible mechanisms were proposed: (a) nanoconfinement will limit the pulverization and destruction of the crystalline structure of anode materials;[2,4,14] (b) interfacial interaction between the oxide and matrix may enhance the intercalation reaction;[8,9,16−18] (c) the irreversible Li$_2$O will gradually decompose into oxide and lithium ion in the presence of Ni in successive charge steps,[19,20] and

(d) the growth of a polymer/gel-like film at low potential may generate an extra capacity.[21]

As the nanoconfinement can prevent the pulverization and/or aggregation of metal oxides during the cycle steps,[15] it is only applied to keep the cyclic stability, but not to explain the anomalous capacity rise.[4] However, in some capacity increase cases, in absence of the catalytic Ni nanoparticles or the matrix of graphene or carbon nanotubes, only pure metal oxides or core/shell nanostructures exist during the charge/discharge cycles, and the final discharge capacity is even higher than the theoretical capacity. Bai et al.[22] fabricated a kind of porous Mn$_3$O$_4$ nanorod by a pyrolysis method, which showed a capacity increment of ca. 100 mAh g$^{-1}$ from the 40$^{th}$ cycle to 150$^{th}$ cycle. They attributed the capacity increment to the surface lithium storage and decomposition of some irreversible Li$_2$O to active lithium and manganese oxide, but no details were discussed to explain the mechanism of the surface lithium storage and the decomposition of irreversible Li$_2$O. Yoon and Manthiram[23] prepared TiO$_2$ core/shell nanostructure anodes, which reached a discharge capacity higher than 200 mAh g$^{-1}$ even after 100 cycles with excellent cyclic stability. In this case, the high cyclic stability of TiO$_2$ was

**Scheme 1. Formation Procedure of CuO@TiO2−NCAs**
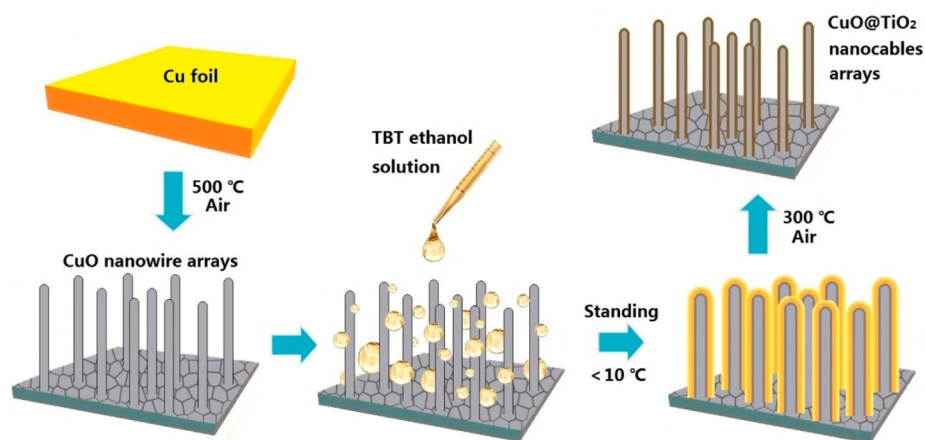


considered to be due to its small crystallite size and large surface area. Also, for these cases, there is no obvious evidence for the formation of polymer/gel-like film being observed. Therefore, more research should be done to explore the reasons for the excellent cyclic performance and extra lithium storage capacity.

In-situ thermal oxidation is a mature technology to prepare CuO nanowires;[24−26] however, the electrochemical performance of these CuO nanowires is very poor. Herein, we use a simple composite process to synthesize a nanocable structure of TiO2-encapsulated CuO nanowires to improve the electrochemical performance of CuO nanowires prepared by in situ thermal oxidation. The lithium insertion material TiO2 is chosen as the "shell" of the CuO@TiO2 nanocable, and its tubular structure, with a higher surface-to-volume ratio, may help to relieve the stress and volume changes occurring during the processes of intercalation and extraction of lithium to maintain its completion.[27] Therefore, the TiO2 nanotube structure will ensure the lithiation reaction of CuO nanowires being confined in a one-dimensional nanospace of the nanotube during the charge−discharge processes. An interesting phenomenon was found in our experiment: as the CuO@TiO2 nanocables with long aspect ratios generate a large CuO/TiO2 phase interface area, the interfacial adsorption during the solid-phase diffusion will propitiously raise the lithium ions' storage capacity to some extent. The experimental results showed that the nanoconfinement effect and the interfacial adsorption have a synergistic effect on improving the lithiation performance of CuO@TiO2 nanocable arrays (CuO@TiO2−NCAs).

## ■ EXPERIMENTAL SECTION

**Preparation of CuO Nanowire Arrays (CuO−NWAs).** A copper foil (99.99% purity) with a thickness of 0.2 mm and a size of 20 × 15 mm$^2$ was first dipped into an aqueous solution of 1 mol L$^{-1}$ HCl for 10 min to purge the oxide layers on the surface; subsequently rinsed in deionized water; cleaned by acetone under an ultrasonic bath for 5 min; and dried in N$_2$ flow afterward. The copper foil was placed in an alumina boat and loaded into a box furnace and annealed at 500 °C for 6 h in air with a heating rate of ∼10 °C min$^{-1}$. CuO−NWAs were formed by this thermal oxidation of the Cu foil.

**Preparation of CuO@TiO2−NCAs.** As illustrated in Scheme 1; a solution of tetrabutyl titanate (TBT) dissolving in ethanol (1:4 v/v) was dropped onto the above thermally treated Cu foil at room temperature; then quickly transferred the sample into a refrigerator; standing at a temperature of less than 10 °C for 1 h. Subsequently, the sample was loaded in a box furnace; and annealed at 300 °C for 4 h under air atmosphere and ambient pressure. The heating rate was kept at ∼10 °C min$^{-1}$. Finally, the brown thin oxide scale was peeled off carefully and set aside.

**Characterization.** The morphologies of CuO−NWAs and CuO@TiO2−NCAs were characterized by field-emission scanning electron microscopy (FE-SEM; Hitachi S-4700) and energy-dispersive X-ray spectroscopy (EDS; attached to SEM). The phase determination was performed by X-ray diffraction (XRD; Rigaku D/max-2500B2+/PCX system with CuKα$\lambda$ = 1.5406 Å; $2\theta$ = 5−90°). X-ray photoelectron spectra (XPS) were recorded on a Thermo Electron Corporation ESCALAB 250 XPS spectrometer. The detail of the microstructures was identified by transmission electron microscopy (TEM; Hitachi H-800) and high-resolution transmission electron microscopy (HRTEM; JEOL JEM-3010F).

**Electrochemical Investigation.** Electrochemical performances of the as-products were measured with two-electrode coin-type cell with lithium foil as counter electrode. The working electrode was prepared by smearing the slurry of 70% active matter, 20% acetylene black, and 10% poly(vinylidene difluoride) in N-methylpyrrolidinone on nickel foam sheets, and drying the working electrode in a vacuum oven at 80 °C for 4 h and then at 120 °C for 12 h. The assembling procedure of the cells was performed in a recirculating argon glovebox, and the electrolyte was a 1 mol L$^{-1}$ LiPF$_6$ solution in a mixture of ethylene carbonate/dimethyl carbonate (1:1 v/v). The galvanostatical charge−discharge tests were carried out in a Land-CT2001A system within the potential range of 0.01−3 V vs Li/Li$^+$ at current densities of 60, 120, 240, 600, 1200, and 2400 mA g$^{-1}$, respectively. Electrochemical impedance spectroscopy (EIS) and cyclic voltammetry (CV) measurements of the working electrode were taken on an electrochemical workstation (CHI 660B). AC impedance spectra were obtained by applying a sine wave with an amplitude of 5.0 mV over a frequency range from 100 kHz to 0.01 Hz. The cyclic voltammograms were obtained over the potential range of 0.01−3 V vs Li/Li$^+$ at a scan rate of 0.1 mV s$^{-1}$.

## ■ RESULTS AND DISCUSSION

In Figure 1, parts a and b, FE-SEM images show that the CuO nanowires grown on the Cu film surface are very dense and of high aspect ratio. The cross-sectional view of CuO−NWAs in Figure 1a illustrates that the nanowires are relatively aligned and almost perpendicular to the oxide scale surface. Most CuO NWs have smooth surfaces and a uniform diameter along their longitudinal axial direction. A statistical measurement shows that the average length and diameter of the nanowires are 6.2 and 0.26 $\mu$m, respectively, and the growth density is ca. 5.13 per $\mu$m$^2$. The TEM image of a randomly selected nanowire illustrated in Figure 1c shows an excellent straightness and a diameter of ca. 175 nm, and no hollow structure is found in the nanowire. Many reports have been focused on the mechanism of the growth of CuO nanowires during the in situ oxidation of metal copper.[28] A cross-sectional view of the oxide layers has illustrated the multilaminate morphology clearly in Figure 1a. The nucleation of
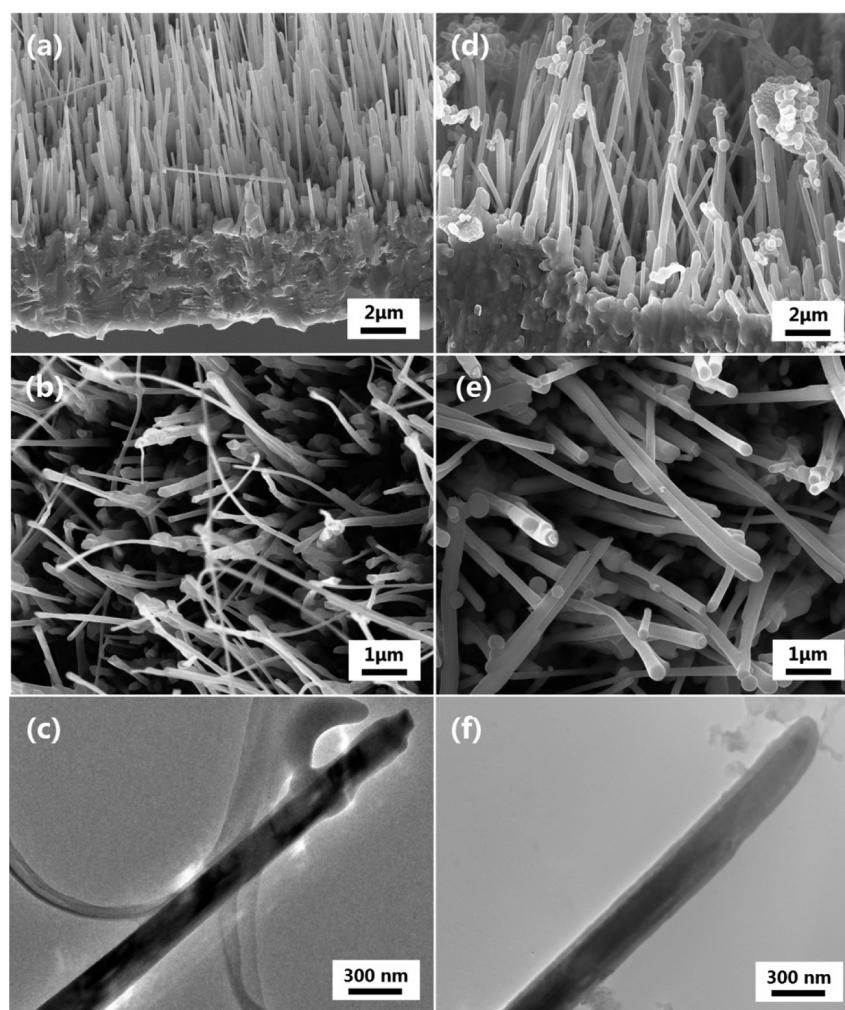
**Figure 1.** SEM images of CuO−NWAs and CuO@TiO$_2$−NCAs: (a) a cross view and (b) a vertical view for CuO−NWAs, (d) a cross view and (e) a vertical view for CuO@TiO$_2$−NCAs; TEM images of CuO−NWAs and CuO@TiO$_2$−NCAs: (c) a single CuO nanowire and (f) a single CuO@TiO$_2$ nanocable.

the nanowires can be treated as a diffusional solid-state transformation process, and its growth is determined by stress-induced short-circuit diffusion.[29]

TBT has been extensively utilized as reactive titanium source to prepare TiO$_2$ nanostructures by the methods of hydrolysis and pyrolysis.[30,31] As the whole reaction is exposed in ambient atmosphere, TBT solution forms liquid membrane around CuO nanowire from tip to root slowly involving a series of complex hydrolysis reaction.[31,32] With the hydrolysis of TBT and the evaporation of ethanol, the liquid membrane around nanowires will solidify to form a solid shell surrounding the CuO nanowires tightly as displayed in Scheme 1. After a calcination treatment, the solid shell will turn into TiO$_2$ completely.[33] The morphologies and structures of CuO@TiO$_2$−NCAs are displayed in Figure 1d−f. A cross-sectional image in Figure 1d shows that nanocables are still perpendicular to the oxide substrate exhibiting an array-like morphology. The smooth surface is kept, but the straightness is slightly decreased compared to CuO nanowires. The morphologies of CuO@TiO$_2$−NCAs are much neater than those of composites in some other reports.[34,35] In Figure 1d, we can see that the CuO nanowires are encapsulated from tip to bottom completely. The average diameter of the nanocables increases to 0.32 $\mu$m from the original 0.26 $\mu$m; however, the growth density decreases to ca. 2.91 per $\mu$m$^2$.

The density decrease may be due to the flow of TBT solution on the CuO−NWAs which will break some of nanowires. A TEM image of a single CuO@TiO$_2$ nanocable is illustrated in Figure 1f, the selected nanocable exhibits an obvious core/shell structure, and the core is wrapped tightly by the outside shell that forms a clearly continuous phase interface. The thickness of the shell is uniform, scrolling into a ring pillar shape.

The CuO−NWAs and CuO@TiO$_2$−NCAs were peeled off from the annealed copper foil and directly used in XRD analysis. It can be seen that CuO−NWAs in Figure 2a exhibit the characteristic peaks of cubic Cu$_2$O phase (JCPDS No. 77-0199) and monoclinic CuO phase (JCPDS No. 80-0076). All the peaks of CuO−NWAs are in good conformability with characteristic peaks of Cu$_2$O and CuO. After transforming into CuO@TiO$_2$−NCAs, the peaks of the CuO phase become stronger and sharper than that of Cu$_2$O, indicating that the amounts of CuO layer and nanowires are greater than that of Cu$_2$O. An XPS measurement was also performed to confirm that the valence state of Cu in CuO@TiO$_2$−NCAs (Supporting Information, SI, Figure S1). The Cu 2p$_{3/2}$ peak is composed of two components at 931.7 and 933.9 eV, corresponding to Cu$_2$O and CuO, respectively.[26] In the XRD pattern of CuO@TiO$_2$−NCAs, two small peaks at 25.3° and 47.9° can be distinguished corresponding to the (101) and (200) planes of TiO$_2$ (anatase). Due to its small amount and low
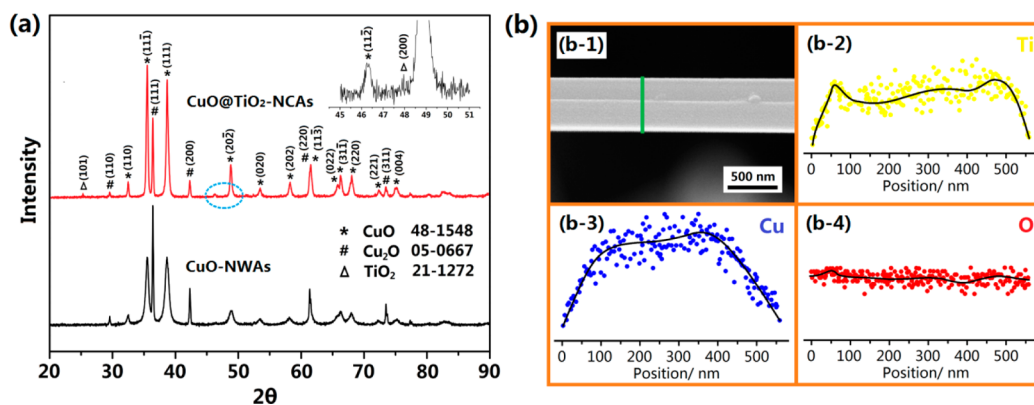
**Figure 2.** (a) XRD patterns of CuO−NWAs and CuO@TiO$_2$−NCAs. The inset image is an enlarged view of the area in azure circle on the pattern of CuO@TiO$_2$−NCAs. (b-1) The electronic image of a single nanocable and its EDX line-scan profiles of (b-2) Ti, (b-3) Cu, and (b-4) O.
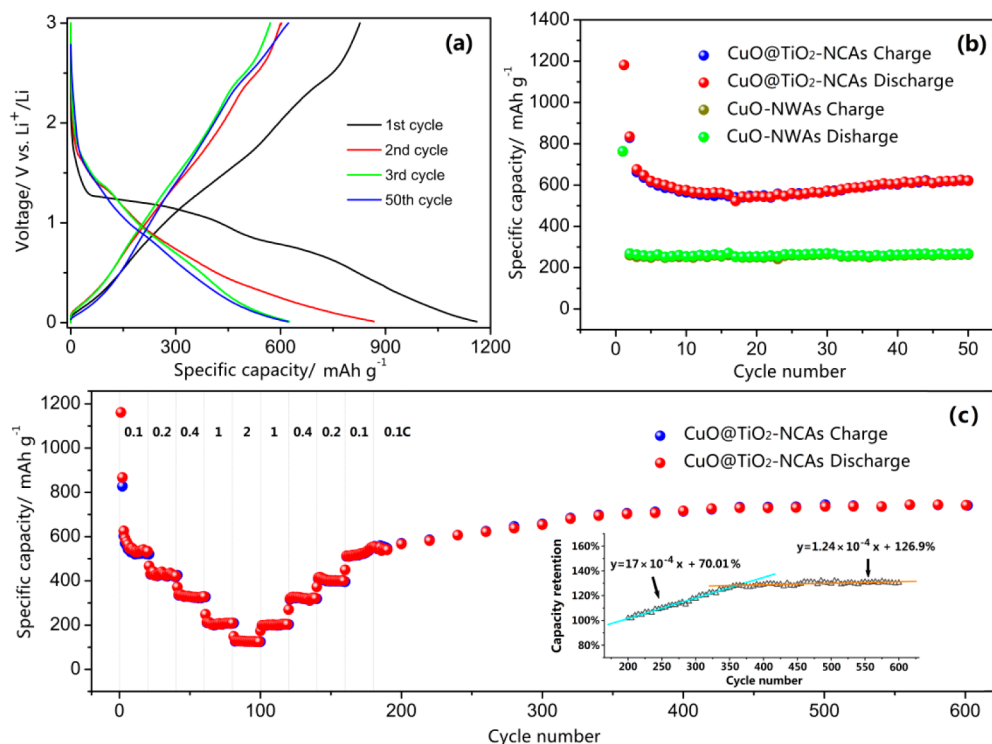


**Figure 3.** (a) Galvanostatic charge−discharge curves of CuO@TiO$_2$−NCAs electrode at the 1$^{st}$, 2$^{nd}$, and 50$^{th}$ cycles; (b) cycling performance of CuO−NWAs and CuO@TiO$_2$−NCAs at 60 mA g$^{-1}$; and (c) capacity retention of CuO@TiO$_2$−NCAs at various current and a continuous long-term cycle performance at 60 mA g$^{-1}$.

oxidation temperature (300 °C), the diffraction peaks of TiO$_2$ are so weak that only the two strongest characteristic peaks can be seen in the XRD pattern. A visualized image on the distribution of each element along the diameter of a nanocable was set up by performing a line-scan profile on a random selected nanocable. The analysis data in Figure 2b show that the nanocable consists of three elements: Ti, Cu, and O. As illustrated in Figure 2(b-2), the distribution of the Ti element shows a typical tubular nano-structure, and the spatial distribution of Cu displaying by blue dots exhibits a cylinder shape. We can conclude that the line-scan results also confirm the CuO core/TiO$_2$ shell nanocable structure.

The lithiation properties of the obtained products were tested by galvanostatical charge−discharge method under various charge rates. The lithiation reaction of CuO as anode is a complex process, which usually can be expressed by three steps.[36] And the lithiation process and properties of anatase have also been

studied widely, and the intercalation reaction can be described as follows[37,38]

$$TiO_2 + xLi^+ + xe^- \rightarrow Li_xTiO_2 \quad 0 \leq x \leq 0.6$$
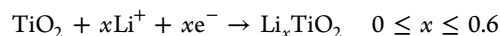
For anatase, $x$ is the mole fraction of Li in TiO$_2$, which typically do not exceed 0.5 during electrochemical insertion,[38] whereas the upper limit is 0.6 for chemical intercalation with butyllithium.[37]

Figure 3a shows the discharge/charge curves of CuO@TiO$_2$−NCAs anode in the first, second, third and 50th cycle at a current density of 60 mA g$^{-1}$. A large specific capacity of 1183 mAh g$^{-1}$ was achieved at the first discharge process (Li-insertion process) with two sloping potential ranges. The potential ranges at 1.31−1.01 V and 0.91−0.01 V are related to the Li intercalation reactions of CuO and Cu$_2$O crystallites, respectively.[17,18] The CV curves of the CuO@TiO$_2$−NCAs anode also confirmed the electrochemical reactions in accordance with the discharge/charge
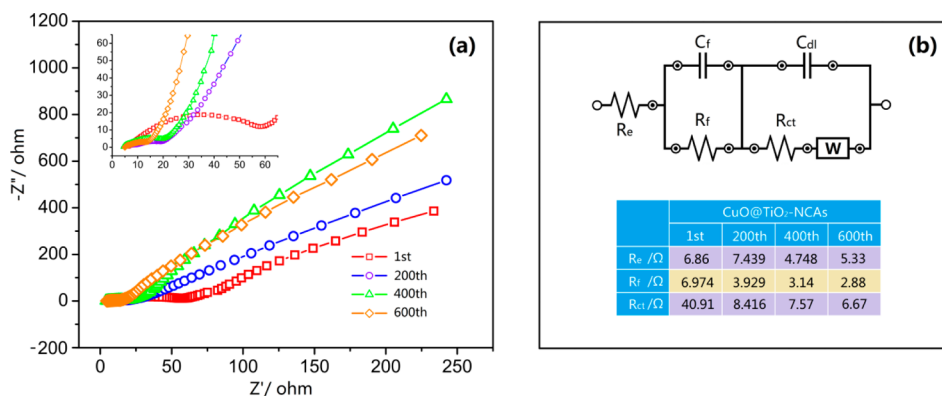
**Figure 4.** (a) AC impedance spectra of CuO@TiO$_2$−NCAs electrode at different cycles (using the same cell in Figure 3c) and (b) the Randles equivalent circuit for the EIS spectra and fitting kinetic parameters for the corresponding components in the circuit.

curves (Figure S2). It can be noticed that the discharge curve with a rapid fall after 3 V experiences a occurrence of inflection around 1.5 V, this may be attributed to the lithiation of anatase.[39] The next cycles, even to the 50th cycle, show narrow sloping potential ranges that emerge in the same voltage scales, respectively, compared to the first cycle, suggesting a high reversibility of lithiation reaction.

Figure 3b illustrates the cycle performances of CuO−NWAs and CuO@TiO$_2$−NCAs electrodes at 60 mA g$^{-1}$. The CuO−NWAs electrode has almost no fading during the first 50 cycles, and the discharge capacities of second cycle and 50th cycle are 268.3 and 267.5 mAh g$^{-1}$, respectively. As an advanced structure, CuO@TiO$_2$−NCAs gives a higher reversible capacity of 663.7 mAh g$^{-1}$. For comparison, the CuO@TiO$_2$−NCAs were also acidified to get the pure TiO$_2$ shell, which shows a reversible capacity of 166 mAh g$^{-1}$ after 50 cycles (Figure S3). We can obtain the initial Coulombic efficiencies of CuO−NWAs and CuO@TiO$_2$−NCAs are 35.2% and 72.2%, respectively, indicates that the CuO@TiO$_2$−NCAs electrode can provide a much higher reversible capacity and lithium utilization efficiency. For both electrodes, the capacity loss in the first cycle can be ascribed to the decomposition of the electrolyte and the subsequent formation of an SEI layer on the electrode surface.[40] All these reactions will generate irreversible Li$_2$O.[41] It is interesting to find that the reversible capacity of CuO@TiO$_2$−NCAs does not always fade but increases gradually after the preceding several cycles. However, this capacity increase phenomenon does not appear in the cycle process of CuO−NWAs. We will give a further investigation by prolonging the cycle number later.

Furthermore, the capacity retention of CuO@TiO$_2$−NCAs was measured at different current densities of 60, 120, 240, 600, and 1200 mA g$^{-1}$, to evaluate its rate performance, and the results are shown in Figure 3c. The CuO@TiO$_2$−NCAs electrode exhibits a good rate capability. When the high current density is reversed back to low current density, the original capacity can be recovered, implying excellent reversibility. The same cell shown in Figure 3c was further tested by a long-term cycle at 60 mA g$^{-1}$, and the capacity continuously increases up to the 190th cycle with a discharge capacity of 543 mAh g$^{-1}$. Here, we set the 190th cycle as an evaluated basic point of the long-term cycle performance. The capacity remains at 716 mAh g$^{-1}$ after 170 cycles, corresponding to a capacity retention of 131.8%, this means a capacity increase of 0.163% per cycle up to the 190th cycle. Then the rising trend slows down and comes into a flat-lined period. The increasing rate has reduced to 0.0046%, correspondingly, the capacity increment is 8 mAh g$^{-1}$ from 360th cycle to 600th cycle. The EDS data showed that the mass ratio of CuO, Cu$_2$O,

and TiO$_2$ in CuO@TiO$_2$−NCAs is 14.4:1:1.8. Accordingly, the theoretical contributions of CuO, TiO$_2$, and Cu$_2$O are 560, 18, and 44 mAh g$^{-1}$, respectively, and the theoretical capacity of CuO@TiO$_2$−NCAs is 622 mAh g$^{-1}$. However, the experimental results showed a reversible capacity of 633 mAh g$^{-1}$, and the value even raised to 716 mAh g$^{-1}$ after 170 cycles. This sign suggests an additional mechanism of lithiation reaction to store more lithium ions, which will be discussed in more details below. From the above results, it is demonstrated that the CuO@TiO$_2$−NCAs electrode shows excellent long-term cyclability and rate-stability performance.

In order to reveal the kinetics of the electrode process, electrochemical impedance spectroscopy (EIS) measurments are carried out. As shown in Figure 4a, the Nyquist plots consist of two semicircles and a linear area. The first depressed semicircle in the high frequency range can be interpreted as the formation of a solid electrolyte interface (SEI) film and migration of lithium ions through the surface films at the electrode/electrolyte interface. The second semicircle appearing at lower frequencies is attributed to the double layer capacity and charge transfer resistance at the electrodes. Semi-infinite diffusion processes in the active material or solid phase of the electrode appear at the low frequency end, exhibiting typical Warburg behaviors in the linear region.[42] A modified Randles equivalent circuit was set up to be the model for EIS analysis to quantify the experimental results,[43] as illustrated in Figure 4b. $R_e$ represents bulk resistance of the cell; $C_f$ and $R_f$ represent the capacitance and resistance of the surface film, respectively; $C_{dl}$ and $R_{ct}$ are the double-layer capacitance related to the nonfaradaic process and the charge-transfer resistance related to the faradaic process, respectively; $W$ is the Warburg impedance related to the diffusion of lithium ions into the bulk electrode. The obtained fitting kinetic parameters of the CuO@TiO$_2$−NCAs electrode are summarized in Figure 4b. It can be seen that both $R_f$ and $R_{ct}$ gradually decrease with the cycle process, implying that the diffusion of lithium ions into the solid phase becomes smoother, and the lithiation reactions of the active material become more facile. The AC impedance spectrum of the CuO−NWAs electrode is also performed, which shows higher impedances than those of the CuO@TiO$_2$−NCAs electrode (Figure S4). The lower $R_{ct}$ of the CuO@TiO$_2$−NCAs electrode implies that the diffusion of lithium ions into the bulk electrode is much more convenient.

The as-produced CuO@TiO$_2$−NCAs in this work show a capacity increase during a long-term cycle, demonstrating a superior cyclability and higher specific capacity than normal CuO−NWAs by in situ thermal oxidation and most other pure

CuO nanostructures.[44] We used TEM measurement to investigate the role of the nanoconfinement effect on improving the electrochemical performance of the $CuO@TiO_2$−NCAs. As illustrated in Figure 5, randomly selected nanocables are in the
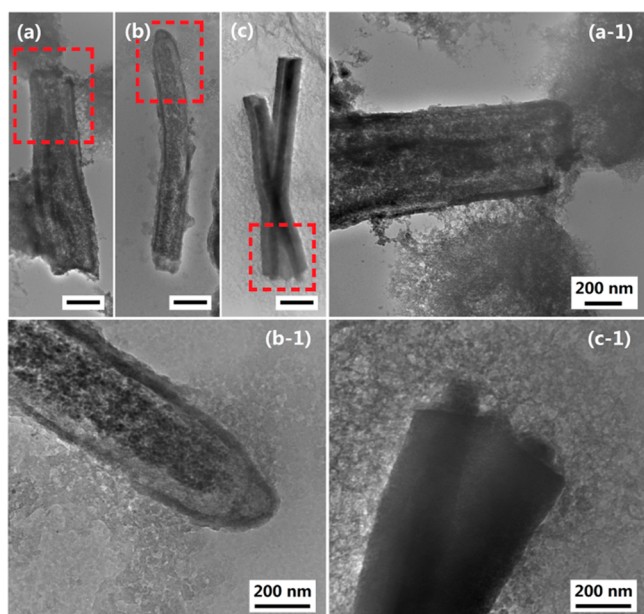


**Figure 5.** TEM images of three typical nanocables after 50 cycles: (a) partial open end type, (b) closed end type, and (c) open end type (scale bars, 500 nm); (a-1), (b-1), and (c-1) are enlarged images of the selected areas in (a), (b), and (c), respectively.

full deintercalation state after cycling. As mentioned earlier, nanocrystalline $TiO_2$ is an insertion material, which means the crystal will not pulverize that easily during the discharge−charge cycle.[27] This is also confirmed in Figure 6, that the $TiO_2$ shell
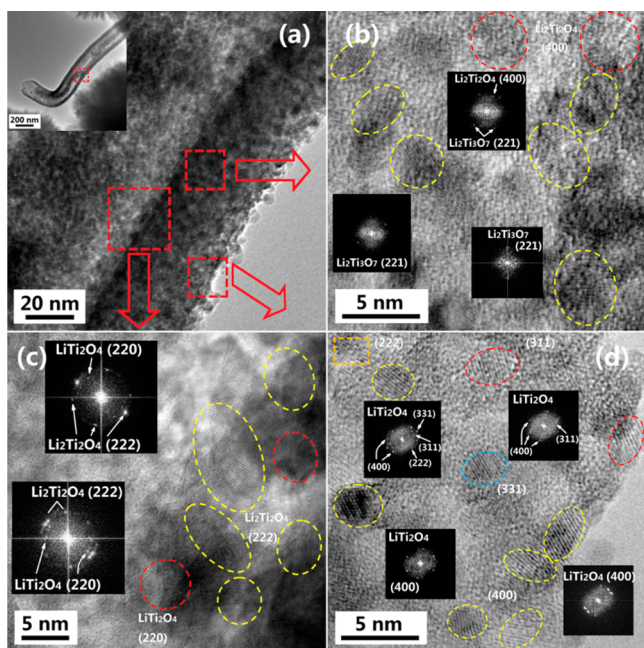


**Figure 6.** HRTEM images of (a) a randomly selected nanocable in a full lithium insertion state and its local features at (b) the interior part near the internal interface, (c) the internal interface, and (d) the external interface of the shell.

remains complete after cycling. We have chosen three typical nanocables: (i) partial open end type, (ii) closed end type, and (iii) open end type. The enlarged images of their end parts are displayed in Figure 5, parts (a-1), (b-1), and (c-1), respectively. CuO is still trapped in $TiO_2$ nanotubes, which hinders CuO from the volume expansion effect and nanocrystalline pulverization, and prolongs the reaction time by preventing the separation of the CuO component from the current collector dispersing into the electrolyte. During the discharge process, the CuO core will be reduced to Cu gradually, which leads to a shrinkage of the core with the formation of a large number of defects in different dimensions (Figure S5). The lithium concentrated reaction mainly focuses on the interfacial side of the $TiO_2$ shell, which may generate numbers of voids.

Although the nanoconfinement from the encapsulated $TiO_2$ shell can prevent the capacity fading, it cannot explain the extra capacity in the long cycling process. However, there is no obvious evidence for the formation of commonly indicated polymer/gel-like films. Therefore, it is necessary to reveal some other reasons for the phenomenon of capacity increase. As is known, plenty of defects exist in dispersing solid−solid interfaces, thus forming enhanced chemical activity sites located at the interfaces,[45,46] which will cause a high interfacial energy.[47−49] According to the theory of interfacial adsorption, the heteroatoms will diffuse to the defects provided by the interfaces to reduce the high interfacial energy.[50] In the case of $CuO@TiO_2$ nanocables, the interfaces between CuO and $TiO_2$ separated from the electrolyte will maintain a much higher interfacial energy.[45,46] As the lithiation reaction continues, the lithium ions diffuse from the external surface of nanocables to the internal core, there will be an extra amount of lithium ions reacting and anchoring at the $CuO/TiO_2$ defect-rich interfaces with chemical activity sites due to the interfacial adsorption effect.[45] It is already known that the intrinsic defect structure of the anatase is dominated by reduction involving the formation of $Ti^{4+}$ and $Ti^{3+}$ polarons, especially at the interfaces there will forms plenty of defect clusters which is helpful to store much more lithium ions.[46,47] XPS also provided the confirmation of the existence of $Ti^{4+}$ and $Ti^{3+}$ defects (Figure S1). We used HRTEM to investigate the interfacial adsorption effect and the formation of new phases. A randomly selected nanocable in a full lithium intercalation state is chosen to be the research subject, as illustrated in the inset image in Figure 6a. Fast Fourier transform (FFT) analysis of the HRTEM image showed that the Li-rich phase is mainly constructed of $Li_2Ti_2O_4$ at the internal interface in Figure 6c, the areas in yellow circles corresponded to $Li_2Ti_2O_4$ (222) fringes with a interplanar spacing of 0.242 nm, and the red circles are $LiTi_2O_4$ (220) fringes with an interplanar spacing of 0.296 nm. The interior part near the internal interface is displayed in Figure 6b, as can be seen in the FFT results, a new phase $Li_2Ti_3O_7$ appears in the areas marked by yellow circles, and is the dominant component in this region. The HRTEM image of a selected area at the external interface illustrated in Figure 6d shows a polycrystalline situation. We directly measured the distances of the fringes in the picture, then texted and verified the results in the FFT pictures, there are four kinds of interplanar spacings, 0.209, 0.255, 0.192, and 0.244 nm, corresponding to the crystal planes (400), (311), (331), and (222) of $LiTi_2O_4$, respectively. No other phase was observed, but $LiTi_2O_4$ at the external interface of the shell. It is found that the internal interface of the $TiO_2$ shell will store more lithium ions by forming Li-richer phases $Li_2Ti_2O_4$ and $Li_2Ti_3O_7$, while the external interface will form $LiTi_2O_4$, which is generally regarded as the maximum insertion phase for electrochemical intercalation.

This may be explained by the interfacial adsorption model aforementioned in this paragraph, which is caused by the high interfacial energy related to the defect structure at the interface.

Other evidence may provide an explanation for the capacity increase. Usually, peaks in the differential $dQ/dV$ curves are indicative of "plateaus" in the charge/discharge curves corresponding to the electrochemical reactions in cells.[37] Here, we chose a series of discharge curves from the long cycle process to investigate their $dQ/dV$ curves, as shown in Figure 7.
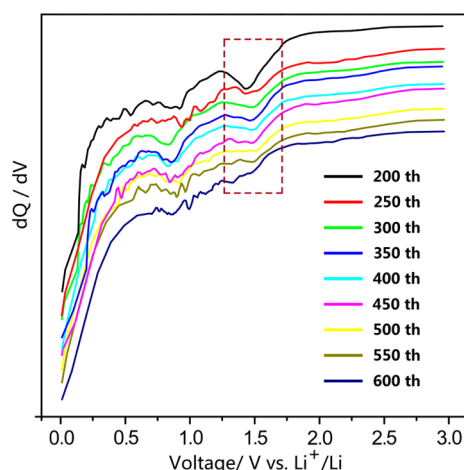


**Figure 7.** Differential capacity vs voltage plots for discharge curves in different cycles of the cell in Figure 3c.

The peaks located above 1.5 V can be regarded as the formation of $LiTi_2O_4$,[39,51] and the peaks at this voltage still existed in the next cycles, which indicated a reversible electrochemical reaction. However, during the following cycles, the left side of the peaks became wider and flatter, and finally gave shoulders, indicating that some other new reactions had widened the peaks. The electrochemical formation of $Li_2Ti_3O_7$ and $Li_2Ti_2O_4$ occur in the range 1.0−1.5 V,[51,52] and with the increase of cycle numbers, these reactions became stronger and stronger to make the left side of the peaks at above 1.5 V into shoulders. These results can also be verified by their excellent conformity with the HRTEM images in Figure 6. Therefore, the extra reversible electrochemical reactions may produce extra capacity.

## CONCLUSIONS

In this work, CuO@TiO$_2$ nanocable arrays were prepared by a simple thermal method and were used as an electrode material for lithium storage. The nanoconfinement effect of CuO@TiO$_2$ nanocables is beneficial for the enhancement of both the cyclability and rate-stability during the long-term charge−discharge process, leading to the excellent electrochemical performance of CuO@TiO$_2$−NCAs with superior reversible capacity of 725 mAh g$^{-1}$ after 400 cycles at a current density of 60 mA g$^{-1}$. For the first time, experimental evidence of interfacial adsorption during the diffusion of lithium ions in a lithiation process was observed, and the interfaces separating from the electrolyte with high interfacial energy will capture more Li-ions and provide extra capacity, which plays a constructive role in lithium storage.

## ASSOCIATED CONTENT

### S Supporting Information

The Supporting Information is available free of charge on the ACS Publications website at DOI: 10.1021/acsami.5b06204.

XPS spectra analysis of CuO@TiO$_2$−NCAs. Cyclic voltammograms of CuO@TiO$_2$−NCAs. Cycle performance of pure TiO$_2$. AC impedance spectra of CuO−NWAs. HRTEM images of the CuO core in fully lithium insertion state (PDF)

## AUTHOR INFORMATION

### Corresponding Author
*Tel: +86 10-64434916; fax: +86 10-64434916; e-mail: songhh@mail.buct.edu.cn (H.S.).

### Notes
The authors declare no competing financial interest.

## ACKNOWLEDGMENTS

## REFERENCES

(1) Poizot, P.; Laruelle, S.; Grugeon, S.; Dupont, L.; Tarascon, J. M. Nano-sized Transition-metal Oxides as Negative-electrode Materials for Lithium-ion Batteries. *Nature* **2000**, *407*, 496−499.

(2) Wang, Z.; Luan, D.; Madhavi, S.; Hu, Y.; Lou, X. Assembling Carbon-coated $\alpha$-Fe$_2$O$_3$ Hollow Nanohorns on the CNT Backbone for Superior Lithium Storage Capability. *Energy Environ. Sci.* **2012**, *5*, 5252−5256.

(3) Lin, F.; Song, H.; Tian, S.; Chen, X.; Zhou, J.; Wang, F. Fe$_{1.5}$Ti$_{0.5}$O$_3$ Nanoparticles as an Anode Material for Lithium-ion Batteries. *Electrochim. Acta* **2012**, *83*, 305−310.

(4) Zhou, J.; Song, H.; Chen, X.; Zhi, L.; Yang, S.; Huo, J.; Yang, W. Carbon-encapsulated Metal Oxide Hollow Nanoparticles and Metal Oxide Hollow Nanoparticles: A General Synthesis Strategy and its Application to Lithium-ion Batteries. *Chem. Mater.* **2009**, *21*, 2935−2940.

(5) Zhang, Z.; Tan, Q.; Chen, Y.; Yang, J.; Su, F. Multiple Transition Metal Oxide Mesoporous Nanospheres with Controllable Composition for Lithium Storage. *J. Mater. Chem. A* **2014**, *2*, 5041−5050.

(6) Zhang, Z.; Ji, Y.; Li, J.; Tan, Q.; Zhong, Z.; Su, F. Yolk Bi-shell Mn$_x$Co$_{1-x}$Fe$_2$O$_4$ Hollow Microspheres and Their Embedded form in Carbon for Highly Reversible Lithium Storage. *ACS Appl. Mater. Interfaces* **2015**, *7*, 6300−6309.

(7) Yang, S.; Song, H.; Yi, H.; Liu, W.; Zhang, H.; Chen, X. Carbon Nanotube Capsules Encapsulating SnO$_2$ Nanoparticles as an Anode Material for Lithium Ion Batteries. *Electrochim. Acta* **2009**, *55*, 521−527.

(8) Wang, X.; Tian, W.; Liu, D.; Zhi, C.; Bando, Y.; Golberg, D. Unusual Formation of $\alpha$-Fe$_2$O$_3$ Hexagonal Nanoplatelets in N-doped Sandwiched Graphene Chamber for High-performance Lithium-ions Batteries. *Nano Energy* **2013**, *2*, 257−267.

(9) Zhang, S.; Zhu, L.; Song, H.; Chen, X.; Zhou, J. Enhanced Electrochemical Performance of MnO Nanowire/graphene Composite during Cycling as the Anode Material for Lithium-ion Batteries. *Nano Energy* **2014**, *10*, 172−180.

(10) Zai, J.; Qian, X. Three Dimensional Metal Oxides−graphene Composites and Their Applications in Lithium Ion Batteries. *RSC Adv.* **2015**, *5*, 8814−8834.

(11) Wang, Z.; Zhou, L. Metal Oxide Hollow Nanostructures for Lithium-ion Batteries. *Adv. Mater.* **2012**, *24*, 1903−1911.

(12) Hu, L.; Chen, Q. Hollow/porous Nanostructures Derived from Nanoscale Metal−organic Frameworks towards High Performance Anodes for Lithium-ion Batteries. *Nanoscale* **2014**, *6*, 1236−1257.

(13) Taberna, P. L.; Mitra, S.; Poizo, P.; Simon, P.; Tarascon, J. M. High Rate Capabilities Fe$_3$O$_4$-based Cu Nano-architectured Electrodes for Lithium-ion Battery Applications. *Nat. Mater.* **2006**, *5*, 567−573.

(14) Wang, Z.; Chen, J.; Lou, X. One-pot Synthesis of Uniform Carbon-coated $MoO_2$ Nanospheres for High-rate Reversible Lithium Storage. *Chem. Commun.* **2010**, *46*, 6906−6908.

(15) Zhang, H.; Song, H.; Chen, X.; Zhou, J. Enhanced Lithium Ion Storage Property of Sn Nanoparticles: the Confinement Effect of Few-walled Carbon Nanotubes. *J. Phys. Chem. C* **2012**, *116*, 22774−22779.

(16) Zhou, J.; Song, H.; Ma, L.; Chen, X. Magnetite/graphene Nanosheet Composites: Interfacial Interaction and Its Impact on the Durable High-rate Performance in Lithium-ion Batteries. *RSC Adv.* **2011**, *1*, 782−791.

(17) Mai, Y. J.; Wang, X. L.; Xiang, J. Y.; Qiao, Y. Q.; Zhang, D.; Gu, C. D.; Tu, J. P. CuO/graphene Composite as Anode Materials for Lithium-ion Batteries. *Electrochim. Acta* **2011**, *56*, 2306−2311.

(18) Yu, Y.; Shi, Y.; Chen, C. H. Nanoporous Cuprous Oxide/lithia Composite Anode with Capacity Increasing Characteristic and High Rate Capability. *Nanotechnology* **2007**, *18*, 055706.

(19) Kang, Y. M.; Kim, K. T.; Kim, J. H.; Kim, H. S.; Lee, P. S.; Lee, J. Y.; Dou, S. X. Electrochemical Properties of $Co_3O_4$, Ni-$Co_3O_4$ Mixture and Ni-$Co_3O_4$ Composite as Anode Materials for Li ion Secondary Batteries. *J. Power Sources* **2004**, *133*, 252−259.

(20) Kang, Y. M.; Kim, K. T.; Lee, K. Y.; Lee, S. J.; Jung, J. H.; Lee, J. Y. Improvement of Initial Coulombic Efficiency of $Co_3O_4$ by Ballmilling Using Ni as an Additive. *J. Electrochem. Soc.* **2003**, *150*, A1538−A1543.

(21) Laruelle, S.; Grugeon, S.; Poizot, P.; Dolle, M.; Dupont, L.; Tarascon, J. M. On the Origin of the Extra Electrochemical Capacity Displayed by MO/Li Cells at Low Potential. *J. Electrochem. Soc.* **2002**, *149*, A627−A634.

(22) Bai, Z.; Zhang, X.; Zhang, Y.; Guo, C.; Tang, B. Facile Synthesis of Mesoporous $Mn_3O_4$ Nanorods as a Promising Anode Material for High Performance Lithium-ion Batteries. *J. Mater. Chem. A* **2014**, *2*, 16755−16760.

(23) Yoon, S.; Manthiram, A. Hollow Core-shell Mesoporous $TiO_2$ Spheres for Lithium Ion Storage. *J. Phys. Chem. C* **2011**, *115*, 9410−9416.

(24) Mumm, F.; Sikorski, P. Oxidative Fabrication of Patterned, Large, Non-flaking CuO Nanowire Arrays. *Nanotechnology* **2011**, *22*, 105605−105610.

(25) Kargar, A.; Jing, Y.; Kim, S.; Riley, C.; Pan, X.; Wang, D. ZnO/CuO Heterojunction Branched Nanowires for Photoelectrochemical Hydrogen Generation. *ACS Nano* **2013**, *7*, 11112−11120.

(26) Liu, Y.; Liao, L.; Li, J.; Pan, C. From Copper Canocrystalline to CuO Nanoneedle Array: Synthesis, Growth Mechanism, and Properties. *J. Phys. Chem. C* **2007**, *111*, 5050−5056.

(27) Song, B.; Liu, S.; Jian, J.; Lei, M.; Wang, X.; Li, H.; Yu, J.; Chen, X. Electrochemical Properties of $TiO_2$ Hollow Microspheres from a Template-free and Green Wet-chemical Route. *J. Power Sources* **2008**, *180*, 869−874.

(28) Filipič, G.; Cvelbar, U. Copper Oxide Nanowires: a Review of Growth. *Nanotechnology* **2012**, *23*, 194001.

(29) Li, A.; Song, H.; Zhou, J.; Chen, X.; Liu, S. CuO Nanowire Growth on $Cu_2O$ by In Situ Thermal Oxidation in Air. *CrystEngComm* **2013**, *15*, 8559−8564.

(30) Shen, J.; Yan, B.; Shi, M.; Ma, H.; Li, N.; Ye, M. One Step Hydrothermal Synthesis of $TiO_2$-reduced Graphene Oxide Sheets. *J. Mater. Chem.* **2011**, *21*, 3415−3421.

(31) Liu, Z.; Zhang, J.; Han, B.; Du, J.; Mu, T.; Wang, Y.; Sun, Z. Solvothermal Synthesis of Mesoporous $Eu_2O_3$-$TiO_2$ Composites. *Microporous Mesoporous Mater.* **2005**, *81*, 169−174.

(32) Chen, X. Q.; Gu, G. B.; Liu, H. B. Reaction of Titanium Tetrabutoxide with Acetic Anhydride and Structure Analysis of the Titanyl Organic Compound Products. *Acta Chim. Sin.* **2003**, *61*, 1592−1596.

(33) Zhang, J.; Li, M.; Feng, Z.; Chen, J.; Li, C. UV Raman Spectroscopic Study on $TiO_2$. I. Phase Transformation at the Surface and in the Bulk. *J. Phys. Chem. B* **2006**, *110*, 927−935.

(34) Jun, J.; Jin, C.; Kim, H.; Park, S.; Lee, C. Fabrication and Characterization of CuO-core/$TiO_2$-shell One-dimensional Nanostructures. *Appl. Surf. Sci.* **2009**, *255*, 8544−8550.

(35) Huang, Q.; Kang, F.; Liu, H.; Li, Q.; Xiao, X. Highly Aligned $Cu_2O$/CuO/$TiO_2$ Core/shell Nanowire Arrays as Photocathodes for Water Photoelectrolysis. *J. Mater. Chem. A* **2013**, *1*, 2418−2425.

(36) Xiang, J. Y.; Tu, J. P.; Qiao, Y. Q.; Wang, X. L.; Zhong, J.; Zhang, D.; Gu, C. D. Electrochemical Impedance Analysis of a Hierarchical CuO Electrode Composed of Self-assembled Nanoplates. *J. Phys. Chem. C* **2011**, *115*, 2505−2513.

(37) Whittingham, M. S.; Dine, M. B. N-Butyllithium an Effective, General Cathode Screening Agent. *J. Electrochem. Soc.* **1977**, *124*, 1387−1388.

(38) Wagemaker, M.; van de Krol, R.; Kentgens, A. P.; Van Well, A. A.; Mulder, F. M. Two Phase Morphology Limits Lithium Diffusion in $TiO_2$ (anatase): A 7Li MAS NMR Study. *J. Am. Chem. Soc.* **2001**, *123*, 11454−11461.

(39) Dambournet, D.; Belharouak, I.; Amine, K. Tailored Preparation Methods of $TiO_2$ Anatase; Rutile, Brookite: Mechanism of Formation and Electrochemical Properties. *Chem. Mater.* **2010**, *22*, 1173−1179.

(40) Debart, A.; Dupont, L.; Poizot, P.; Leriche, J. B.; Tarascon, J. M. A Transmission Electron Microscopy Study of the Reactivity Mechanism of Tailor-made CuO Particles Toward Lithium. *J. Electrochem. Soc.* **2001**, *148*, A1266−A1274.

(41) Wu, G. T.; Wang, C. S.; Zhang, X. B.; Yang, H. S.; Qi, Z. F.; Li, W. Z. Lithium Insertion into CuO/carbon Nanotubes. *J. Power Sources* **1998**, *75*, 175−179.

(42) Yan, J.; Song, H.; Yang, S.; Yan, J.; Chen, X. Preparation and Electrochemical Properties of Composites of Carbon Nanotubes Loaded with Ag and $TiO_2$ Nanoparticle for Use as Anode Material in Lithium-ion Batteries. *Electrochim. Acta* **2008**, *53*, 6351−6355.

(43) Yang, S.; Song, H.; Chen, X. Electrochemical Performance of Expanded Mesocarbon Microbeads as Anode Material for Lithium-ion Batteries. *Electrochem. Commun.* **2006**, *8*, 137−142.

(44) Li, A.; Song, H.; Wan, W.; Zhou, J.; Chen, X. Copper Oxide Nanowire Arrays Synthesized by In-situ Thermal Oxidation as an Anode Material for Lithium-ion Batteries. *Electrochim. Acta* **2014**, *132*, 42−48.

(45) Nowotny, M. K.; Sheppard, L. R.; Bak, T.; Nowotny, J. Defect Chemistry of Titanium Dioxide. Application of Defect Engineering in Processing of $TiO_2$-based Photocatalysts. *J. Phys. Chem. C* **2008**, *112*, 5275−5300.

(46) Olson, C. L.; Nelson, J.; Islam, M. S. Defect Chemistry; Surface Structures; and Lithium Insertion in Anatase $TiO_2$. *J. Phys. Chem. B* **2006**, *110*, 9995−10001.

(47) Hasigaowa, G.; Xi, W.; Shimou, C.; Yoshio, B.; Dmitri, G. Coaxial Cu-Si@C Array Electrodes for High-performance Lithium Ion Batteries. *Chem. Commun.* **2011**, *47*, 12098−12100.

(48) Barnard, A. S.; Curtiss, L. A. Prediction of $TiO_2$ Nanoparticle Phase and Shape Transitions Controlled by Surface Chemistry. *Nano Lett.* **2005**, *5*, 1261−1266.

(49) Wang, X.; Weng, Q.; Liu, X.; Wang, X.; Tang, D.; Tian, W.; Zhang, C.; Yi, W.; Liu, D.; Bando, Y.; Golberg, D. Atomistic Origins of High Rate Capability and Capacity of N-doped Graphene for Lithium Storage. *Nano Lett.* **2014**, *14*, 1164−1171.

(50) Kingery, W. D. Metal-ceramic Interactions: IV. Absolute Measurement of Metal-ceramic Interfacial Energy and the Interfacial Adsorption of Silicon from Iron-silicon Alloys. *J. Am. Ceram. Soc.* **1954**, *37*, 42−45.

(51) Gover, R. K.; Tolchard, J. R.; Tukamoto, H.; Murai, T.; Irvine, J. T. Investigation of Ramsdellite Titanates as Possible New Negative Electrode Materials for Li Batteries. *J. Electrochem. Soc.* **1999**, *146*, 4348−4353.

(52) Kuhn, A.; Baehtz, C.; Garcia-Alvarado, F. Structural Evolution of Ramsdellite-type $Li_xTi_2O_4$ upon Electrochemical Lithium Insertion-deinsertion ($0 \leq x \leq 2$). *J. Power Sources* **2007**, *174*, 421−427.